Supplementary Information (SI) for Lab on a Chip.

Dynamic Gap Structure for High-Throughput Measurement of Cellular Mechanical Properties

Doudou Ma [a,b], Nobutoshi Ota [b], Masaya Taniguchi [c], Yu-Hau Ye [c], Yuri Ito [b], Kazunori Okano [c], Naomi Tanga [c], Yoichiroh Hosokawa [c], Kazuya Sakai [d], Yo Tanaka [b], Koki Yamamoto [b]*, Yaxiaer Yalikun [c]*

[a] *Graduate School of Frontier Biosciences, The University of Osaka, Japan*

[b] *Center for Biosystems Dynamics Research, RIKEN, Japan*

[c] *Medelux research center, NARA Institute of Science and Technology, Japan*

[d] *Department of Blood Transfusion Medicine, Nara Medical University, Kashihara, Japan*

Device Fabrication

Device fabrication was carried out with minor modifications based on our previous report.

1. Photomask Preparation

An aluminum layer was deposited onto a photomask substrate by electron-beam evaporation (EB1200, Canon Anelva Corp., Kanagawa, Japan).

2. Substrate Cleaning and Metal Deposition

Glass substrates (30 × 70 × 0.7 mm) were cleaned by mechanical polishing followed by piranha solution treatment (H_2SO_4:H_2O_2 = 3:1, v/v) for 15 min.

Subsequently, chromium (Cr) and gold (Au) layers were deposited onto the cleaned glass surface using an Electron Cyclotron Resonance (ECR) ion beam sputtering system (EIS-220, Elionix, Tokyo, Japan). The thicknesses of the Cr and Au layers were 73 nm and 65 nm, respectively.

3. Photolithography and Wet Etching

A positive photoresist (OFPR-800) was spin-coated at 2000 rpm for 25 s, followed by soft baking at 96 °C for 90 s.

The resist-coated substrate was exposed to UV light through a photomask using a mask aligner (MA-10, Mikasa, Japan) to define the microchannel pattern (26 mm length × 800 µm width).

After exposure, the pattern was developed using tetramethylammonium hydroxide (TMAH, Tokuyama Corp., Tokyo, Japan). The exposed Cr/Au layers were subsequently removed using appropriate etchants.

Glass etching was performed using an aqueous solution of HF (20 wt%) and HCl (2 wt%), resulting in microchannels with dimensions of 800 µm width and 30 µm height. The channel lengths were designed as 5 mm and 21 mm for different sections.

After etching, the remaining photoresist was removed using acetone, followed by oxygen plasma cleaning.

4. Weir Structure Fabrication

The weir structure (1 mm length × 800 µm width × 1 µm depth) was fabricated on the same substrate using electron-beam (EB) lithography and reactive ion etching (RIE).

An EB resist was spin-coated at 1000 rpm for 60 s and baked at 180 °C for 2 min, yielding a thickness of approximately 550 nm. A charge dissipation layer was applied to minimize charging during EB exposure.

Pattern writing was performed using an EB lithography system (ELS-7500, Elionix, Tokyo, Japan) at an acceleration voltage of 50 kV and a beam current of 300 pA, with an exposure dose of 90 $\mu C/cm^2$.

The exposed resist was developed in o-xylene for 4 min. The pattern was transferred into the glass substrate using an inductively coupled plasma reactive ion etching (ICP-RIE) system (EIS-700, Elionix, Japan) with SF_6 gas. The antenna RF power and bias RF power were set to 500 W and 100 W, respectively, with an SF_6 flow rate of 10 sccm.

5. Port Formation

Inlet and outlet ports were fabricated using a 0.8 mm mechanical drill.

6. Bonding Process

Prior to bonding, glass substrates were manually polished using a melamine resin pad and treated with piranha solution for surface activation.

A 700 μm-thick glass substrate and a 30 μm-thick glass sheet were manually aligned under running water and fixed using binding clips. The assembly was dried at room temperature for 24 h to achieve initial bonding.

Finally, the bonded device was annealed at 110 °C for 3 h to enhance bonding strength.

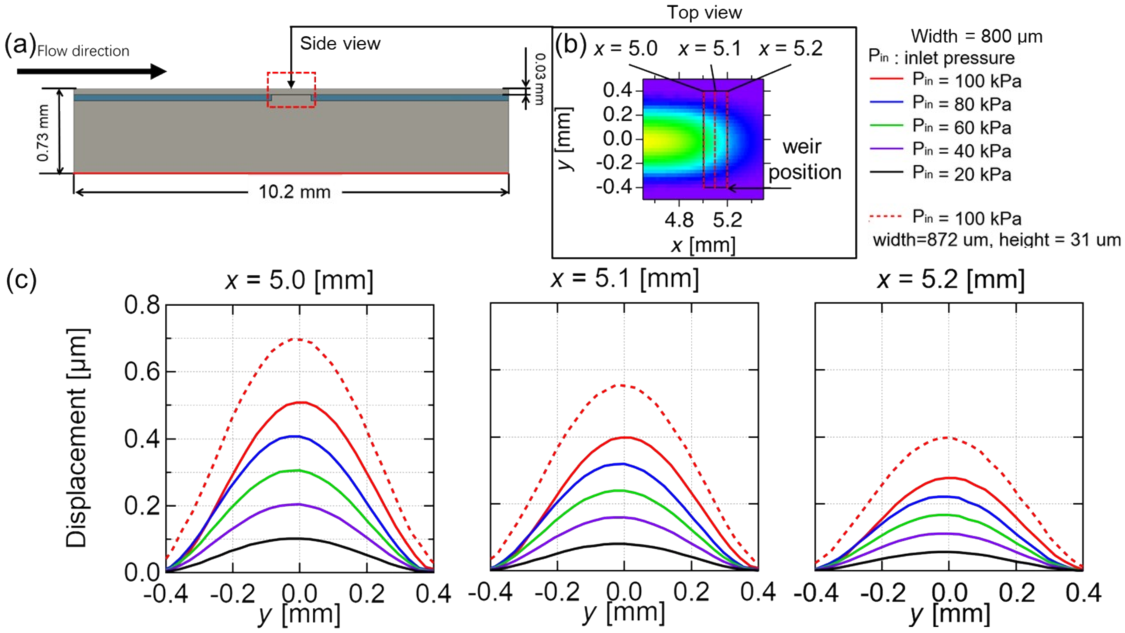

Figure S1. Simulation results of the fluid–structure interaction analysis. (a) Computational domain used for the FSI simulation, consisting of approximately 1 million finite-element mesh elements and representing a straight microfluidic channel with dimensions of 800 μm (width) × 30 μm (height) × 10.2 mm (length). (b) The ultra-thin glass forming the Dynamic Gap Structure (DGS) was modeled as a solid elastic membrane with a thickness of 30 μm and a width of 800 μm, positioned on top of the weir from x = 5.0 mm to 5.2 mm (corresponding to a 200 μm length). A uniform pressure ranging from 10 to 100 kPa was applied to evaluate pressure-induced deformation. (c) To account for fabrication tolerances and possible bonding variations, the channel width w was treated as a parametric variable with values of 800 μm (ideal design) and 872 μm (measured width including fabrication error). For the widest channel, at 100 kPa (w = 872 μm), the maximum membrane deformation reached approximately 0.7 μm at x = 5.0 mm, 0.55 μm at x = 5.1 mm, and 0.4 μm at x = 5.2 mm. Including the original gap height of 1 μm, the corresponding effective gap heights increased to approximately 1.7 μm, 1.55 μm, and 1.4 μm, respectively.

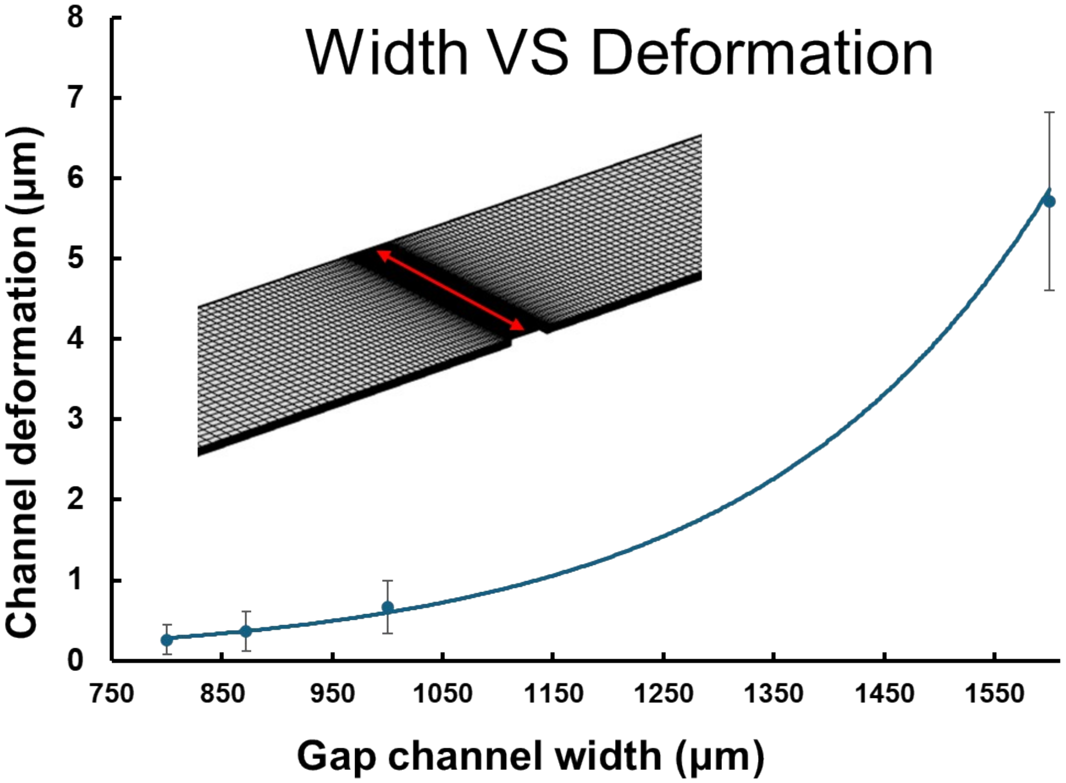

Figure S2. Simulation results showing the effect of channel width on gap deformation.

At an applied pressure of 100 kPa, increasing the channel width leads to a pronounced increase in the maximum deformation of the dynamic gap structure. The peak deformation increases from approximately 260 nm to ~7 μm, resulting in an effective gap height that expands from 1.26 μm to ~8 μm, relative to the original gap height of 1 μm.

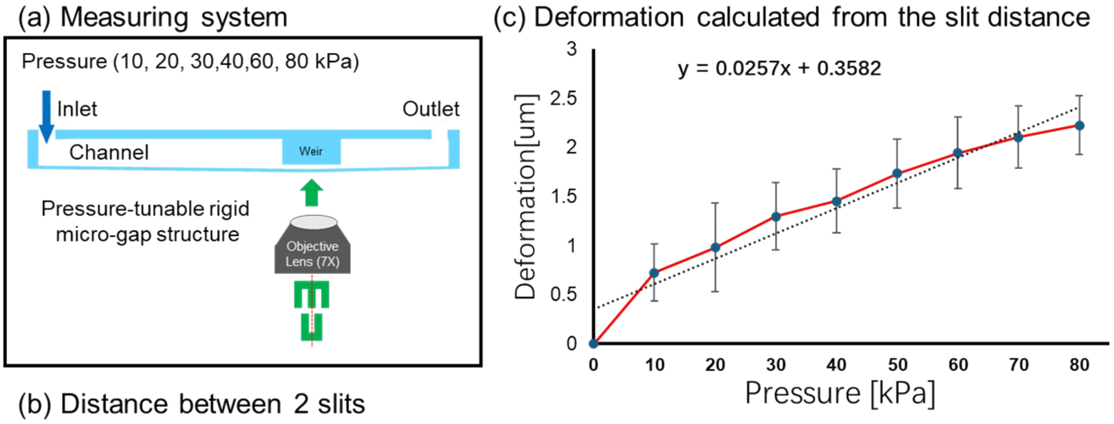

(a) Measuring system

(c) Deformation calculated from the slit distance

(b) Distance between 2 slits

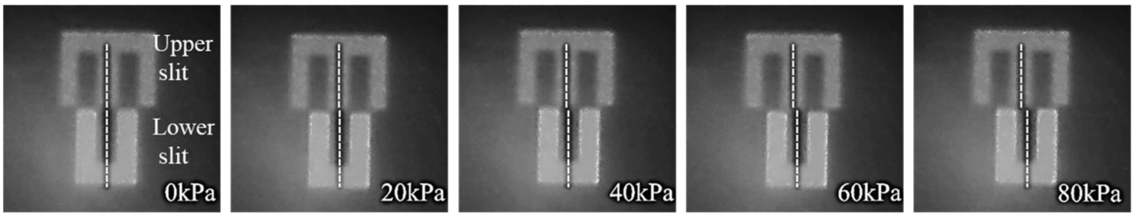

Figure S3. Focus-pilot-unit-based measurement of gap deformation.

(a) Schematic of the optical measurement principle, in which a two-part slit pattern is projected onto the sample surface along the optical axis of the microscope.

(b) Increasing gap deformation induces a linear separation of the two initially aligned slit patterns. By calibrating the separation distance between the slit images, the vertical displacement (height change) of the deformed surface can be quantitatively determined.

(c) Measured gap deformations as a function of applied pressure. At pressures of 10, 20, 30, 40, 50, 60, 70, and 80 kPa, the corresponding deformations were approximately 0.70, 0.98, 1.20, 1.40, 1.70, 1.90, 2.10, and 2.20 μm, respectively.

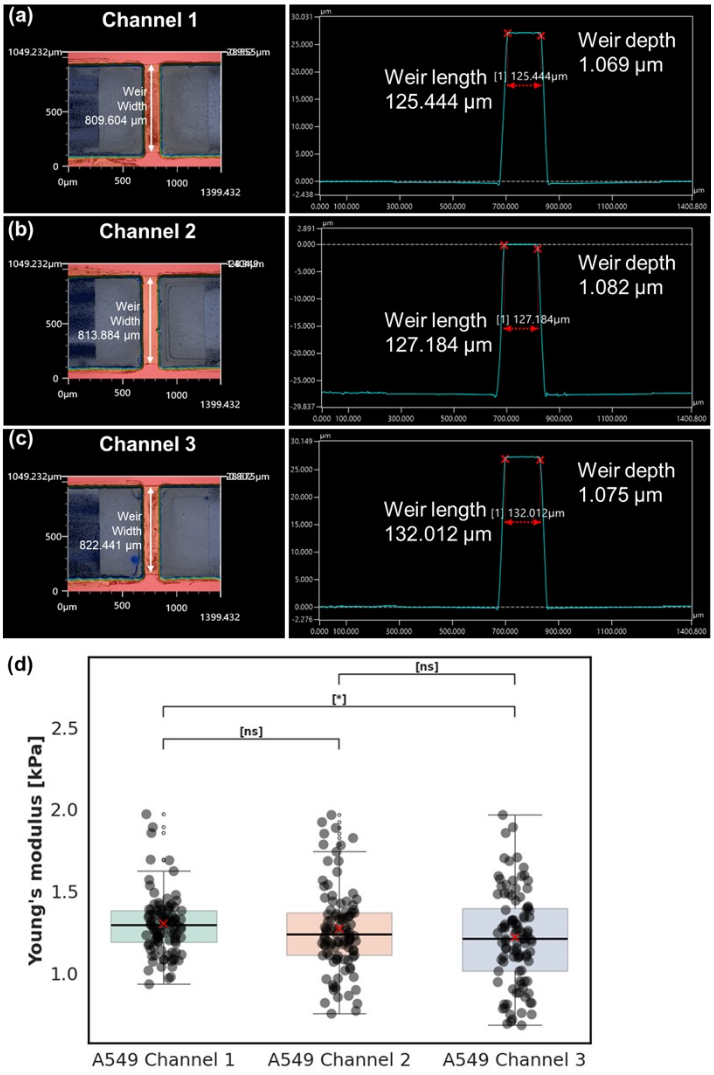

Figure S4. Device-to-device variation and measurement reproducibility of the DGS platform.

(a–c) Optical images (left) and corresponding surface profiles (right) of the weir structures in three independently fabricated channels (Channel 1–3). The weir widths are 809.604 μm, 813.884 μm, and 822.441 μm for Channels 1–3, respectively. The extracted weir lengths are 125.444 μm, 127.184 μm, and 132.012 μm, with corresponding gap depths of 1.069 μm, 1.082 μm, and 1.075 μm, demonstrating high geometric consistency across devices. (d) Young's modulus distributions of untreated A549 cells measured using the three channels. The results show substantial overlap with similar median values, indicating good reproducibility of the mechanical measurements. Statistical analysis reveals no significant difference (ns) between Channel 1 and Channel 2, and between Channel 2 and Channel 3, while a minor but statistically significant difference (*) is observed between Channel 1 and Channel 3. Overall, the variation between devices is small compared to the intrinsic biological variability, confirming the robustness of the DGS platform. N=100.

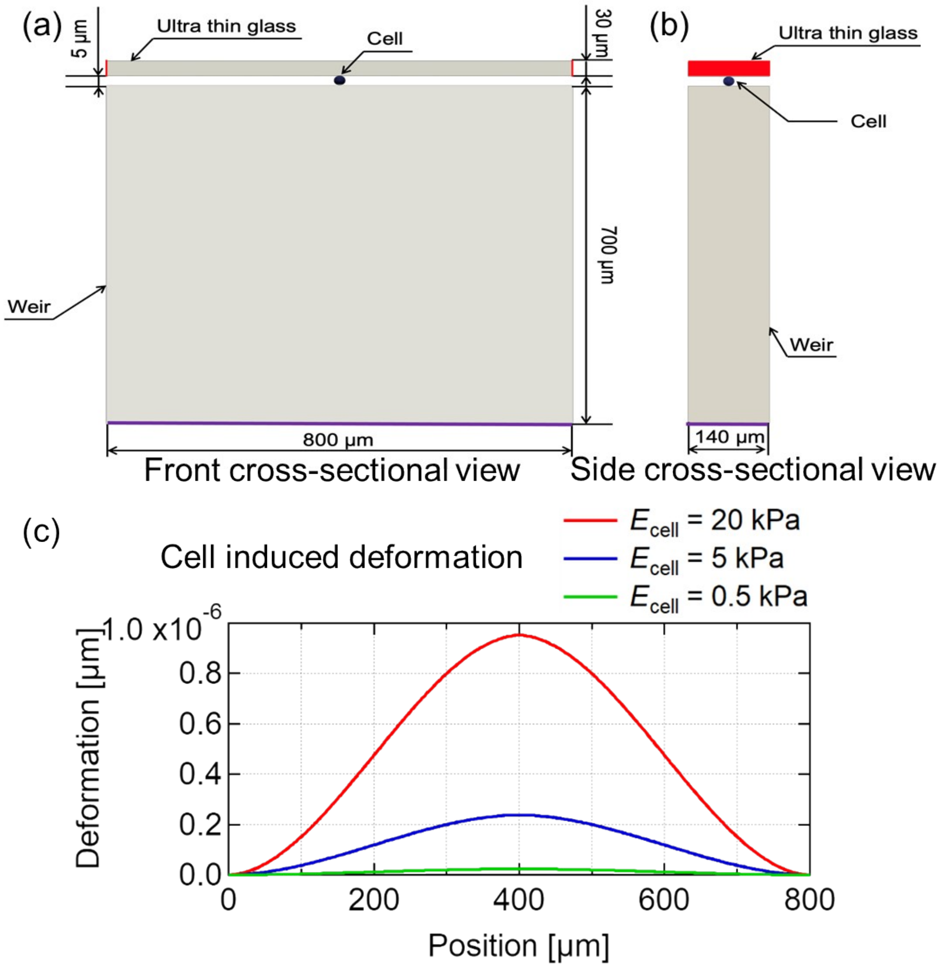

Figure S5. Fluid–structure interaction (FSI) simulation of cell-induced deformation in the dynamic gap structure (DGS). (a) Front cross-sectional view and (b) side cross-sectional view of the simulation model, illustrating the ultra-thin glass membrane, weir structure, and a deformable cell positioned within the gap region. The geometric parameters of the device are indicated. (c) Simulated deformation profiles of the glass membrane along the channel length for cells with different elastic moduli (E_cell = 20 kPa, 5 kPa, and 0.5 kPa). The results show that the additional deformation induced by the presence of the cell is extremely small (on the order of 10^{-6} μm) and strongly dependent on cell stiffness.

These results indicate that the deformation of the dynamic gap is dominated by the externally applied pressure, while the mechanical interaction between the cell and the glass membrane has a negligible effect. This supports the validity of the pressure-based stress estimation used for calculating the apparent Young’s modulus.

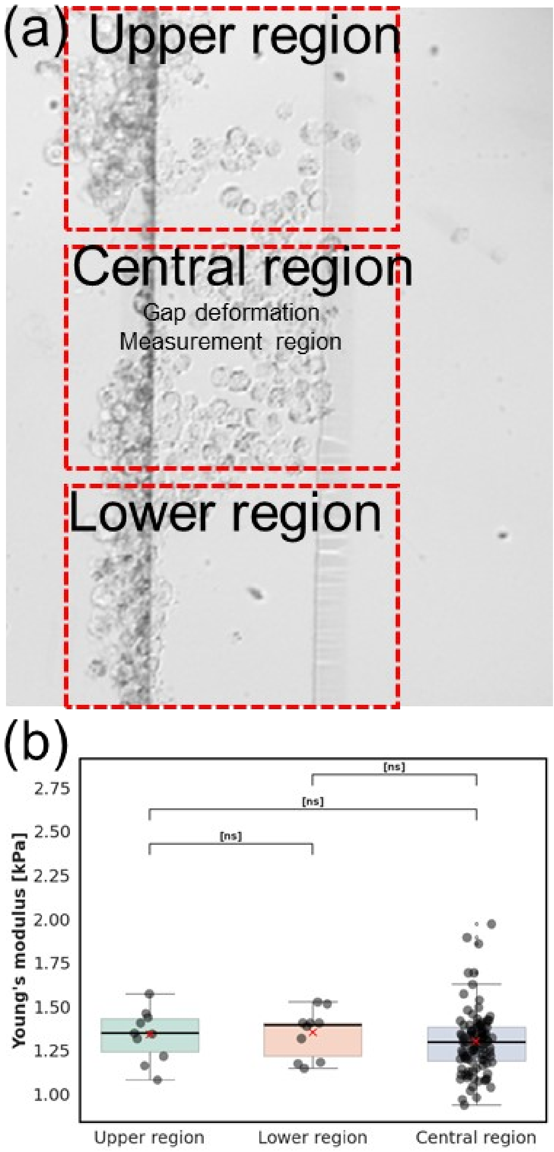

Figure.S6. Spatial verification of gap deformation and measurement consistency across different regions of the device. (a) Representative microscopic image showing three regions along the gap structure: upper, central, and lower regions. The central region corresponds to the gap deformation measurement area where most of the cells pass through the constriction. (b) Comparison of the Young's modulus of A549 cells measured in the upper, central, and lower regions. The results show substantial overlap with similar median values, and statistical analysis indicates No Significant differences (ns) among the regions. These findings confirm that the central measurement region provides representative and stable mechanical characterization, and that potential edge effects do not significantly influence the measured results.

Experimental details clogging inducing:

HL-60 cells were cultured in RPMI 1640 (Nacalai Tesque) supplemented with 10% FBS at 37 °C and 5% CO_2. Non-filtered cell suspensions (concentration: 5×10^5 cells mL^{-1}) were introduced into the device and continuously measured for > 40 min.

The operating pressure at pressure controller was 10 kPa, with clog-recovery and refresh pressures set to 20 kPa and 35 kPa, respectively.

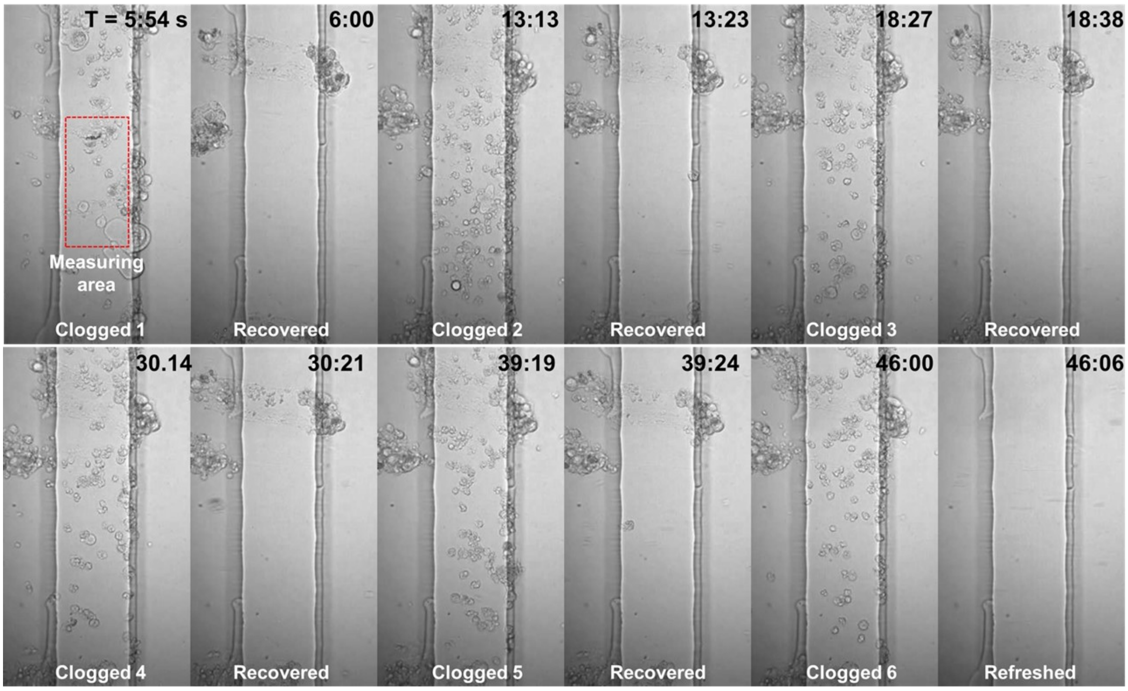

Figure.S7. Demonstration of clogging and rapid recovery in the dynamic gap structure (DGS). Time-lapse images showing 6 clogging event and subsequent recovery during continuous operation. At T=0 s, cells accumulate near the gap entrance, forming a temporary blockage. Upon applying a transient increase in pressure (approximately 20kPa), the adaptive gap expands, allowing the obstructing cells to pass through and restoring flow within a few seconds. A subsequent higher-pressure pulse (approximately 35kPa) fully clears residual cells and refreshes the channel for continued measurement. These results demonstrate the strong clog resistance and rapid recovery capability of the DGS under high-throughput conditions.